energies

MDPI

Article

High-Frequency LLC Resonant Converter with GaN Devices and Integrated Magnetics

Yu-Chen Liu [1,*], Chen Chen [2], Kai-De Chen [2], Yong-Long Syu [2] and Meng-Chi Tsai [1]

1. Department of Electrical Engineering, National Ilan University, No. 1 Section 1 Shennong Road, Yilan 260, Taiwan; kid3181910@gmail.com
2. Department of Electronic Engineering, National Taiwan University of Science, and Technology, No. 43 Section 4 Keelung Rd Da'an District, Taipei 10607, Taiwan; D10502204@mail.ntust.edu.tw (C.C.); d10502203@mail.ntust.edu.tw (K.-D.C.); x452800@gmail.com (Y.-L.S.)

* Correspondence: ycliu@niu.edu.tw

Received: 15 April 2019; Accepted: 5 May 2019; Published: 10 May 2019

check for updates

Abstract: In this study, a light emitting diode (LED) driver containing an integrated transformer with adjustable leakage inductance in a high-frequency isolated LLC resonant converter was proposed as an LED lighting power converter. The primary- and secondary-side topological structures were analyzed from the perspectives of component loss and component stress, and a full-bridge structure was selected for both the primary- and secondary-side circuit architecture of the LLC resonant converter. Additionally, to achieve high power density and high efficiency, adjustable leakage inductance was achieved through an additional reluctance length, and the added resonant inductor was replaced with the transformer leakage inductance without increasing the amount of loss caused by the proximity effect. To optimize the transformer, the number of primary- and secondary-side windings that resulted in the lowest core loss and copper loss was selected, and the feasibility of the new core design was verified using ANSYS Maxwell software. Finally, this paper proposes an integrated transformer without any additional resonant inductor in the LLC resonant converter. Transformer loss is optimized by adjusting parameters of the core structure and the winding arrangement. An LLC resonant converter with a 400 V input voltage, 300 V output voltage, 1 kW output power, and 500 kHz switching frequency was created, and a maximum efficiency of 97.03% was achieved. The component with the highest temperature was the transformer winding, which reached 78.6 °C at full load.

Keywords: LLC resonant converter; integrated transformer; adjustable leakage inductance; LED driver

1. Introduction

Light emitting diode (LED) lighting has become more popular in recent years, particularly as product energy efficiency has become more important to consumers [1–3]. Compared with conventional lighting equipment, LEDs are brighter and have a longer service life. LEDs have thus been used in various lighting scenarios, such as street lighting, indoor lighting, and backlighting. They have also been used for lighting equipment with high power requirements, like baseball field or basketball court lights. Most of these LED driver circuits have a two-stage architecture consisting of a power factor correction converter in the first stage and an isolated buck converter in the second stage, with an LLC resonant converter usually employed as the second-stage circuit [4,5].

Unlike other common isolated buck converters, an LLC resonant converter is characterized by power components with zero voltage switching (ZVS) and zero current switching at the high—and low—voltage ends, respectively, in a full load range. Additionally, unlike phase-shifted full-bridge converters, an LLC converter has no output inductance at the low-voltage end and thus has higher conversion efficiency [6]. Moreover, to achieve high power density, increasing the switching frequency of the power switch reduces the volume of the magnetic component; however, this is accompanied by a considerable increase in switching loss. Therefore, in addition to the ZVS feature of the LLC resonant converter, wide-band-gap switch components should also be employed to reduce the switching loss under high-frequency operation [7,8]. Additionally, selecting an appropriate LLC resonant converter architecture can further optimize the efficiency and reduce component stress [9–11]. The topologies commonly used in the high-voltage end of the LLC resonant converter are the half bridge and full bridge, whereas those used in the low-voltage end are the full bridge or center tap.

To achieve high power density, the leakage inductance of the transformer in this study was used as the resonant inductor of the circuit [12–14], which reduces the number of magnetic components required. Previous research replaced the resonant inductor with the leakage inductance of the transformers, mostly through winding the transformer using litz wire and setting the operating frequency between 50 and 200 kHz. However, when the operating frequency is between 500 kHz and 1 MHz, the litz wire is usually replaced by printed circuit board (PCB) windings to reduce the alternating-current (AC) resistance of the copper traces under high-frequency operation. Additionally, the primary- and secondary-side windings are interleaved to weaken the proximity effect. This approach reduces proximity-effect-induced loss and minimizes the leakage inductance of the transformer [15–17], which is a disadvantage in LLC resonant converters that require leakage inductance to design resonant tanks. A conventional method for increasing the leakage inductance is to increase the spacing between the primary and secondary sides [18–20], which is mostly achieved using a non-interleaved winding that leads to a sharp rise in the proximity-effect-induced AC loss. Therefore, the concept of adjustable leakage inductance [21,22] was adopted in this study, with an additional reluctance length added between the primary-side and secondary-side windings of the transformer. This enabled the magnetic flux generated by the primary-side winding to flow into the added reluctance length, thereby increasing the primary-side leakage inductance. The proposed approach weakens the proximity effect in the interleaved winding and attains the objective of increasing the leakage inductance. Compared to existing LED power converter designs [23–25], this work reduces the switching loss via wide bandgap devices and soft switching techniques under 500 kHz switching frequency conditions and utilizes an integrated transformer without an additional resonant inductor to achieve high power density. Ultimately, an LLC resonant converter with an output power of 1 kW, switching frequency of 500 kHz, input voltage of 400 V, and output voltage of 300 V was achieved in this study.

In this study, a second-stage LLC resonant converter was proposed for the LED driver circuit, and the LLC resonant circuit was used as a direct-current transformer (DCX) to operate the driver circuit at high efficiency. In addition, this study also designed and optimized the primary- and secondary-side topologies and magnetic components in the LLC resonant converter. In Section 2, under the conditions of 1 kW output power, 400 V input voltage, and 300 V output voltage, the loss and component stress at the primary—and secondary—side structures of the converter are analyzed and a topology suitable for the specification in this study is selected. Section 3 details the mathematical induction of adjustable leakage inductance and the appropriate number of primary- and secondary-side windings for the new core based on the optimal point of core loss and copper loss. The feasibility of the designed core structure was verified using ANSYS Maxwell software (ANSYS, Canonsburg, PA, USA). Section 4 presents the experimental results, including temperature distribution maps.

2. LLC Topology Comparison

The primary and secondary sides of different architectures are discussed in this section. Because different circuit specifications have their appropriate architecture, the architecture is chosen based on power level and component stress, as shown in Figure 1. The primary side may consist of a half bridge or full bridge, whereas the secondary side comprises a center-tap and full-bridge rectification. The choice of different architectures for the primary side results in different transformer designs; hence, the primary side is mainly selected based on the corresponding architecture for the appropriate power level. As for the different architectures on the secondary side, there are different component stresses and numbers of switches. Therefore, the appropriate architecture for the secondary side is mainly selected according to the level of the output voltage and current.

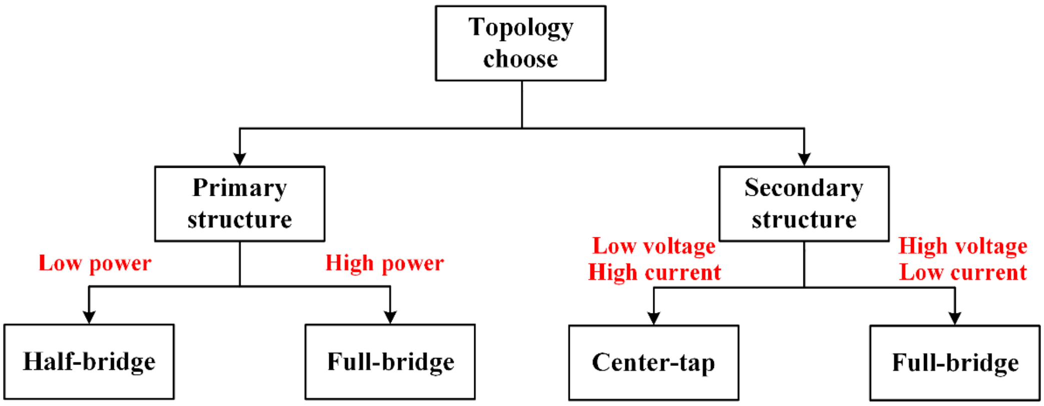

Figure 1. Architecture selection diagram.

The common structures for the primary side are the half bridge and full bridge (Figure 2). For the half bridge, the voltage across the resonant tank is $+V_{in}$ to 0 V; however, the actual voltage across the transformer is $\pm V_{in}/2$. Therefore, the turns ratio between the primary and secondary sides must be accounted for when designing the transformer. The energy transfer formula in Equation (1) can be rewritten as a general formula that establishes ZVS under a half-bridge structure, as shown in Equation (2).

$$\frac{1}{2}LI^2 \geq \frac{1}{2}CV^2 \tag{1}$$

in which the unit of L is Henry (H), I is Ampere (A), C is Farad (F), and V is Volt (V).

$$L_m \leq \frac{t_{dead}}{16C_{oss}f_{sw}} \tag{2}$$

in which the unit of L_m is Henry (H), t_{dead} is seconds (s), C_{oss} is Farad (F), and f_{sw} is Hertz (Hz).

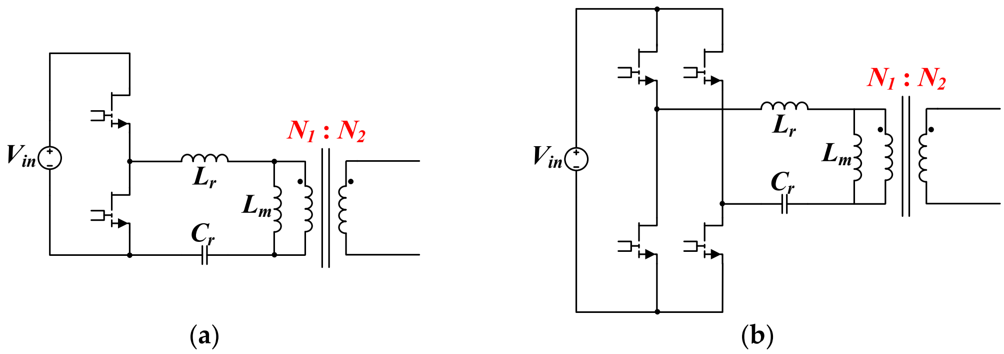

Figure 2. Primary structure (**a**) half bridge and (**b**) Full bridge topology.

For a full-bridge structure, the voltage across the transformer is approximately $\pm V_{in}$, and the input voltage can be directly divided by the output voltage to obtain the turns ratio when designing the transformer. For primary-side switching to achieve ZVS in a full-bridge structure, the energy transfer formula Equation (1) can be rewritten as the following general formula:

$$L_m \leq \frac{t_{dead}}{8C_{oss}f_{sw}} \tag{3}$$

Under the conditions of 400 V input voltage, 300 V output voltage, and a half-bridge structure of the primary side, the equivalent turns ratio of the primary and secondary sides is indicated by Equation (4), whereas Equation (5) obtains the equivalent turns ratio of the two sides when a full-bridge structure is adopted on the primary side. In choosing the primary-side architecture, the conditions of primary-side ZVS are influenced by the stray capacitance [26]. In particular, the stray capacitance of the secondary side mapped back to the primary side is affected by the turns ratio. Thus, if a half-bridge structure was adopted under this specification, the stray capacitance mapped from the secondary to the primary side would be magnified. Therefore, a full-bridge structure was employed in this study to reduce the effect on ZVS condition. Table 1 [27] shows a comparison of the various ratings of the two primary-side architectures.

$$\frac{N_1}{N_2} = \frac{V_{in}/2}{V_o} = \frac{2}{3} \tag{4}$$

$$\frac{N_1}{N_2} = \frac{V_{in}}{V_o} = \frac{4}{3} \tag{5}$$

Table 1. Comparison of primary-side architectures.

Primary Structure	Half-Bridge	Full-Bridge
Primary device voltage stress	V_{in} (400 V)	V_{in} (400 V)
Primary device current stress	$\frac{V_o\sqrt{4\pi^2+\left(\frac{N_1}{N_2}\right)^4 R_L{}^2\left(\frac{T}{Lm}\right)^2}}{4\cdot\frac{N_1}{N_2}\cdot R_L}$ (8.25 A)	$\frac{V_o\sqrt{4\pi^2+\left(\frac{N_1}{N_2}\right)^4 R_L{}^2\left(\frac{T}{Lm}\right)^2}}{4\cdot\frac{N_1}{N_2}\cdot R_L}$ (4.81 A)
Primary device rms current	$\frac{V_o\sqrt{4\pi^2+\left(\frac{N_1}{N_2}\right)^4 R_L{}^2\left(\frac{T}{Lm}\right)^2}}{8\cdot\frac{N_1}{N_2}\cdot R_L}$ (4.08 A)	$\frac{V_o\sqrt{4\pi^2+\left(\frac{N_1}{N_2}\right)^4 R_L{}^2\left(\frac{T}{Lm}\right)^2}}{8\cdot\frac{N_1}{N_2}\cdot R_L}$ (2.36 A)
Resonant inductor rms current	$\frac{V_o\sqrt{4\pi^2+\left(\frac{N_1}{N_2}\right)^4 R_L{}^2\left(\frac{T}{Lm}\right)^2}}{4\sqrt{2}\cdot\frac{N_1}{N_2}\cdot R_L}$ (5.8 A)	$\frac{V_o\sqrt{4\pi^2+\left(\frac{N_1}{N_2}\right)^4 R_L{}^2\left(\frac{T}{Lm}\right)^2}}{4\sqrt{2}\cdot\frac{N_1}{N_2}\cdot R_L}$ (3.38 A)
ZVS condition	$L_m \leq \frac{t_{dead}}{16C_{oss}f_{sw}}$	$L_m \leq \frac{t_{dead}}{8C_{oss}f_{sw}}$
Turns ratio	N_1:N_2 (12:18)	N_1:N_2 (24:18)
Primary device	GS66508B, 650 V	GS66508B, 650 V
Number of primary device	2	4
Total SR conduction loss	$I_{rms}{}^2 \cdot R_{ds(on)} \cdot 2$ (1.665 W)	$I_{rms}{}^2 \cdot R_{ds(on)} \cdot 4$ (1.114 W)
Winding loss of primary side	7.24 W	5.51 W
Proper specification	Low power	High power

In Table 1, T is the switching period, and its unit is seconds (s), and RL is the output load. Its unit is Ohm (Ω). ZVS, zero voltage switching. SR, synchronous rectifier.

Common structures for the secondary side are center-tap and full-bridge rectification (Figure 3). For center-tap rectification, the voltage over the secondary side of the transformer was $1 \times V_o$; however, the voltage over the synchronous rectifiers (SRs) was $2 \times V_o$, and overall, the conduction loss amounted to that of two SRs. Based on this analysis, the center-tap structure was more suitable for low-output-voltage and high-current specifications.

Compared with those in the center-tap structure, the voltage over the secondary side and the SRs of the transformer in the full-bridge rectification structure were $1 \times V_o$; however, the conduction loss amounted to that of four SRs. Based on this analysis, full-bridge rectification was suitable for high-output-voltage and low-current specifications. For the high-output-voltage specification and considering the tradeoff between the SR voltage rating, SR conduction loss, and secondary-side copper loss, full wave rectification was selected for the secondary-side structure, and the switch employed was the GS66508B. Table 2 shows a comparison of the SR rated voltage, transformer turns ratio, and SR number of the two secondary-side architectures.

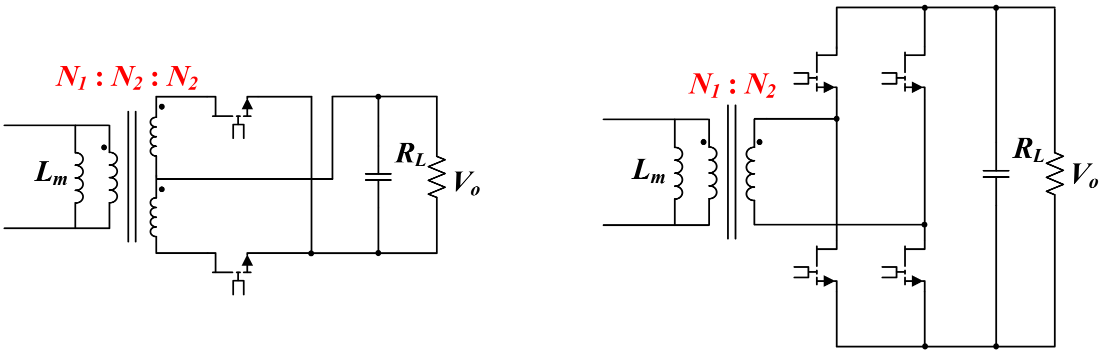

(**a**) (**b**)

Figure 3. Secondary-side architecture: (**a**) center tap and (**b**) full bridge.

Table 2. Comparison of secondary-side architectures.

Secondary Structure	Center-Tap	Full-Bridge
SR voltage stress	$2\ V_0$ (600 V)	V_0 (300 V)
SR current stress	$\sqrt{12}\dfrac{V_o\sqrt{12\pi^4+\frac{5\pi^2-48}{Lm^2}\left(\frac{N_1}{N_2}\right)^4 R_L{}^2T^2}}{24\pi R_L}$ (5.5 A)	$\sqrt{12}\dfrac{V_o\sqrt{12\pi^4+\frac{5\pi^2-48}{Lm^2}\left(\frac{N_1}{N_2}\right)^4 R_L{}^2T^2}}{24\pi R_L}$ (5.5 A)
SR rms current	$\sqrt{3}\dfrac{V_o\sqrt{12\pi^4+\frac{5\pi^2-48}{Lm^2}\left(\frac{N_1}{N_2}\right)^4 R_L{}^2T^2}}{24\pi R_L}$ (2.67 A)	$\sqrt{3}\dfrac{V_o\sqrt{12\pi^4+\frac{5\pi^2-48}{Lm^2}\left(\frac{N_1}{N_2}\right)^4 R_L{}^2T^2}}{24\pi R_L}$ (2.67 A)
Turns ratio	N1:N2:N2 (24:18:18)	N1:N2 (24:18)
SR device	GS66508B, 650 V	GS66508B, 650 V
Number of SR device	2	4
Total SR conduction loss	${I_{rms}}^2 \cdot R_{ds(on)} \cdot 2$ (0.713 W)	${I_{rms}}^2 \cdot R_{ds(on)} \cdot 4$ (1.426 W)
Winding loss of secondary side	2.41 W	2.41 W
Proper specification	Low output voltage High output current	High output voltage Low output current

Next, the differences between the four architectures (primary and secondary side) are compared. In terms of the primary-side switch voltage stress, both the half bridge and full bridge result in a voltage stress of $1 \times V_{in}$, whereas the secondary-side switch voltage stress is $2\ V_o$ and V_o for center-tap and full-bridge rectification, respectively. The voltage over the transformer was $\pm 0.5\ V_{in}$ when a half-bridge structure was employed for the primary side, whereas using a full-bridge structure yielded a voltage of $\pm V_{in}$. Therefore, when transmitting the same power, the transformer current was I_r when a full-bridge structure was used on the primary side but had to be $2\ I_r$ if a half-bridge structure was used. Because the voltage over the transformer was half the input voltage, the current on the primary side was greater when a half-bridge structure was employed than when the primary side comprised a full-bridge structure. Therefore, the primary-side half-bridge architecture is suitable for circuits with low power applications to prevent excessive current flow through the transformer, which would result in saturation. Regarding the secondary side, the component voltage stress when the center-tap structure was used was twice that when full-bridge rectification was employed, whereas the number of components was half; the center-tap structure is thus appropriate for low-voltage-output and high-current applications. Table 3 shows a comparison of the characteristics for the four architectures.

Table 3. Comparison of the four architectures.

Component	**Primary Side: Half-Bridge Secondary Side: Center-Tap**	**Primary Side: Half-Bridge Secondary Side: Full-Bridge**	**Primary Side: Full-bridge Secondary side: Center-Tap**	**Primary side: Full-Bridge Secondary side: Full-Bridge**
Primary device voltage stress	V_{in}	V_{in}	V_{in}	V_{in}
SR voltage stress	2 V_0	V_0	$2V_0$	V_0
Primary-side transformer voltage stress	±0.5 V_{in}	±0.5 V_{in}	$\pm V_{in}$	$\pm V_{in}$
Secondary-side transformer voltage stress	$\pm V_0$	$\pm V_0$	$\pm V_0$	$\pm V_0$
Primary-side transformer current	2 I_r	2 I_r	I_r	I_r
Proper specification	Low power Low output voltage High output current	Low power High output voltage Low output current	High power Low output voltage High output current	High power High output voltage Low output current

The loss distribution of the four architectures was calculated on the basis of the specifications in this study (Figure 4). According to the loss distribution illustrated in Figure 4, the loss of each architecture type was mostly copper loss of the transformers and other loss types, including the equivalent series resistance of the capacitor and via loss. The overall efficiency of the architecture comprising a primary-side full-bridge structure and secondary-side center-tap structure was the highest of all architectures. However, because the specification of this study was high output voltage, the SR voltage rating of the secondary-side center-tap structure had to be 2 V_o; additionally, the actual test circuit was not ideal. Therefore, the architecture with primary-side full-bridge and secondary-side full bridge structures, which had the second highest efficiency, was selected to prevent the SR from being damaged by the high voltage.

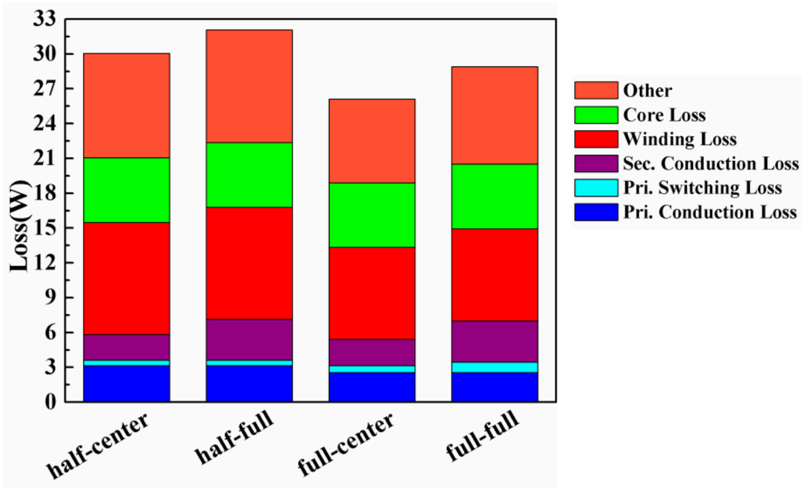

Figure 4. Comparison of loss types in different architectures.

3. Design Concept and Loss Optimization of Adjustable Leakage Inductance

The conventional integrated leakage inductance is formed by leakage flux that is lost to the air and does not pass through the secondary side. Accurate control of the amount of leakage inductance is practically difficult. The concept of adjustable leakage inductance that was adopted in this study was to add an additional reluctance length that prevents some flux generated on the primary side from flowing into the secondary-side winding, in turn generating leakage inductance. The leakage inductance used in this study was designed using the concept of split flow of the transformer reluctance.

Figure 5 presents the concept of adjustable leakage inductance, where the voltage of the primary side and secondary side are denoted by Vp and Vs, respectively. The winding in the primary side was divided into two parts, of which one part wound counterclockwise with 18 turns around the left outer leg, and the other wound clockwise with 6 turns around the right outer leg. Similarly, the winding on the secondary side was also divided into two parts, in which one part wound clockwise with 6 turns around the left outer leg, and the other wound counterclockwise with 12 turns around the right outer leg. Moreover, according to Equation (6), the magnetomotive force (MMF) of these windings could be represented as 18 I_p, 6 Is, 6 Ip, and 12 I_s, and their voltage as V_{pw}, V_{px}, V_{sy}, and V_{sz}, respectively. R_o represents the reluctance of the outer leg, and R_c represents the reluctance of the center leg.

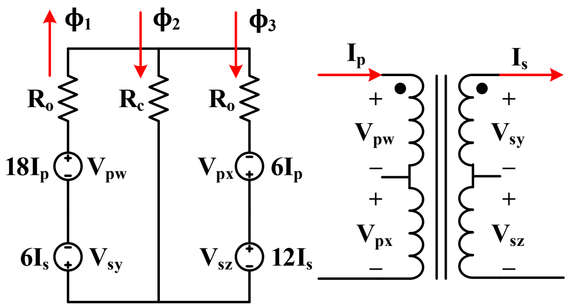

Figure 5. Reluctance model for adjustable leakage inductance.

$$\phi = \frac{mmf}{R} = NI \tag{6}$$

Figure 6 displays the equivalence of the reluctance generated by the passing flux produced in the left leg that was achieved by using the superposition theorem. Regarding the core structure, because the reluctances of both outer legs are the same, the equivalent reluctance passing through ϕ_1 and ϕ_3 are the same, as indicated in Equation (7). After the reluctance passing through the flux has been obtained,

ϕ_1 could be presented as Equation (8); although the equivalent reluctance *of* ϕ_1 and $\phi_{3\neg}$ are the same, ϕ_3 could be presented as in Equation (9) because the MMF is different for each leg. Because the center leg had no windings, only the values of flux on the left and right outer legs are listed.

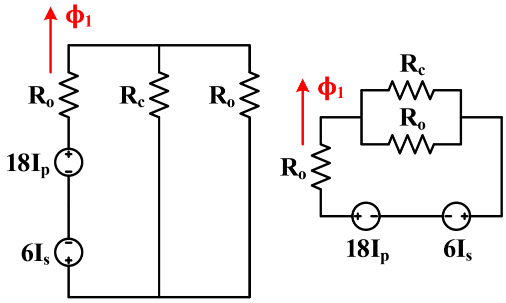

Figure 6. Equivalent reluctance model for flux split flow.

$$R_{\phi 1} = R_{\phi 3} = \frac{R_o(R_o + 2R_c)}{R_o + R_c} \tag{7}$$

$$\phi_1 = \left(18I_p - 6I_s\right) \cdot \frac{R_o + R_c}{R_o(R_o + 2R_c)} \tag{8}$$

$$\phi_3 = \left(6I_p - 12I_s\right) \cdot \frac{R_o + R_c}{R_o(R_o + 2R_c)} \tag{9}$$

As mentioned, the MMF generated from the windings on each leg was determined using the superposition theorem. Subsequently, Equations (10)–(12) represent the total flux of each leg in consideration of flux split flow.

$$\phi_{1\_total} = \frac{18R_o + 24R_c}{R_o(R_o + 2R_c)} \cdot I_p - \frac{6R_o + 18R_c}{R_o(R_o + 2R_c)} \cdot I_s \tag{10}$$

$$\phi_{2\_total} = \frac{12}{R_o(R_o + 2R_c)} \cdot I_p - \frac{6}{R_o(R_o + 2R_c)} \cdot I_s \tag{11}$$

$$\phi_{3\_total} = \frac{6R_o + 24R_c}{R_o(R_o + 2R_c)} \cdot I_p - \frac{12R_o + 18R_c}{R_o(R_o + 2R_c)} \cdot I_s \tag{12}$$

According to Figure 7, the primary-side voltage of the transformer V_p is the sum of V_{pw} and V_{px}; the secondary-side voltage of the transformer V_s is the sum of V_{sy} and V_{sz}. As demonstrated by Equation (13), Faraday's law of induction was employed to ascertain the relationship between the voltage, number of turns, and variation in flux over time. Moreover, the primary-side voltage V_p and secondary-side voltage V_s of the transformer are represented using Equations (14) and (15).

$$V = n\frac{d\phi}{dt} \tag{13}$$

$$V_p = \frac{360R_o + 576R_c}{R_o(R_o + 2R_c)} \cdot \frac{dI_p}{dt} - \frac{180R_o + 432R_c}{R_o(R_o + 2R_c)} \cdot \frac{dI_s}{dt} \tag{14}$$

$$V_s = \frac{180R_o + 432R_c}{R_o(R_o + 2R_c)} \cdot \frac{dI_p}{dt} - \frac{180R_o + 324R_c}{R_o(R_o + 2R_c)} \cdot \frac{dI_s}{dt} \tag{15}$$

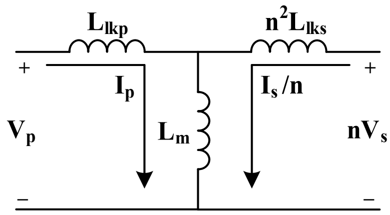

Figure 7. T model of the transformer.

By using Faraday's law of induction to assess the relationship between the voltage, reluctance, and number of turns of the transformer, the T model of the transformer (Figure 7) could be applied. In Figure 7, V_p refers to the primary-side voltage of the transformer, and V_s refers to the secondary-side voltage of the transformer; furthermore, L_{lkp} represents the primary-side leakage inductance, L_{lks} represents the secondary-side leakage inductance, and L_m represents the excitation inductance of the transformer. The T model enabled the equivalence of the voltage, current, and leakage inductance of the secondary side with that of the primary side. Equations (16) and (17) present the results.

$$V_p = \left(L_m + L_{lkp}\right)\frac{dI_p}{dt} - \left(\frac{L_m}{n}\right)\frac{dI_s}{dt} \tag{16}$$

$$V_s = -\left(\frac{L_m}{n}\right)\frac{dI_p}{dt} + \left(\frac{L_m}{n^2} + L_{lks}\right)\frac{dI_s}{dt} \tag{17}$$

Subsequently, Equations (14) and (16) could be compared with Equations (15) and (17). Equations (18)–(20) represent the relationship among the leakage inductance and excitation inductance of the primary and secondary sides of the transformer and the number of turns of the windings.

$$L_m + L_{lkp} = \frac{360R_o + 576R_c}{R_o(R_o + 2R_c)} \tag{18}$$

$$\frac{L_m}{n} = \frac{180R_o + 432R_c}{R_o(R_o + 2R_c)} \tag{19}$$

$$\frac{L_m}{n^2} + L_{lks} = \frac{180R_o + 324R_c}{R_o(R_o + 2R_c)} \tag{20}$$

The comparison could be used to establish models of equivalent leakage inductance of the primary and secondary sides of the transformer and the excitation inductance. Such models could be presented using Equations (21)–(23).

$$L_m = \frac{240R_o + 576R_c}{R_o(R_o + 2R_c)} \tag{21}$$

$$L_{lkp} = \frac{120R_o}{R_o(R_o + 2R_c)} \tag{22}$$

$$L_{lks} = \frac{45R_o}{R_o(R_o + 2R_c)} \tag{23}$$

According to the obtained results, a three-legged core could achieve adjustable leakage inductance if the shape of the outer legs easily enables winding. Applying the winding coil is difficult when the commonly used PQ and RM cores are employed because of their outer leg shape; thus, EI or EE cores were used for adjustable leakage inductance [21]. The simulation results of the current distribution of the PCB trace windings based on the shapes of the PQ and EI cores were obtained with Maxwell magnetic simulation software. The simulation results presented in Figure 8 yielded the winding for the square core, and the current distribution obtained using the square core was considerably more uneven than that obtained using the round core, leading to excessively dense current at the corner of the winding, hot spots, and higher losses. Therefore, the cylindrical core was selected as the transformer core in this study.

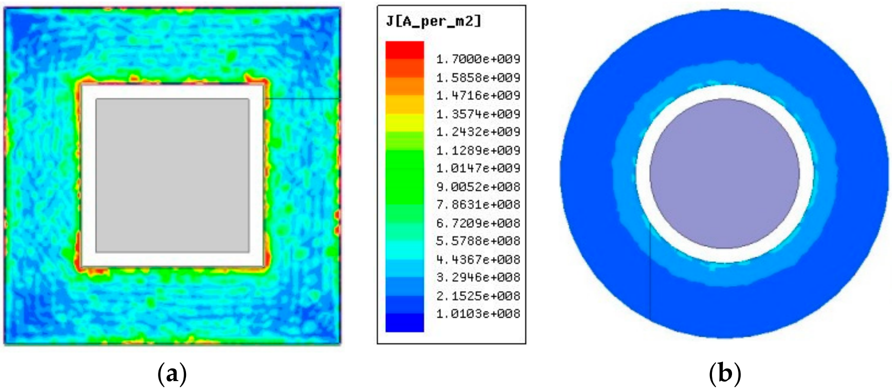

Figure 8. Relationship between the winding shapes of effective core cross sections and current distribution: (**a**) square-shaped cross section; (**b**) round cross section.

The design presented in Figure 9 was proposed to achieve adjustable inductance through winding on the two outer legs of the three-legged core and the obtainment of even current distributions on PCB windings. Producing adjustable leakage inductance required that windings be set only on the outer legs and not on the center leg. This method enabled the cross-sectional area of the center leg to be altered to a shape suitable for PCB winding, increasing the effectiveness of the winding space of the transformer. Therefore, this study proposed aligning two PQ cores (Figure 9a), where the connected part serves as the center leg of the core, and removal of one outer leg of the original core forms a new three-legged structure for the core. The design is as presented in Figure 9b.

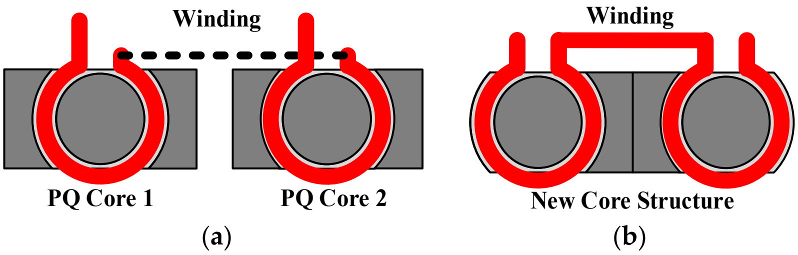

Figure 9. Diagram of the innovative core structure: (**a**) PQ core structure; (**b**) the innovative core structure.

Figure 10 shows a diagram of the core size design in this study. Figure 10a is the top view, and *r* represents the radius of the effective cross-sectional area, *R* denotes the radius of the core that can be wound, *l* is twice the horizontal distance from the core cylinder to the highest point of the center leg, *m* is the maximum width of the center leg, *n* is the length of the core, *d* is the thickness of the top and bottom pieces, and *t* represents the leg height of the core.

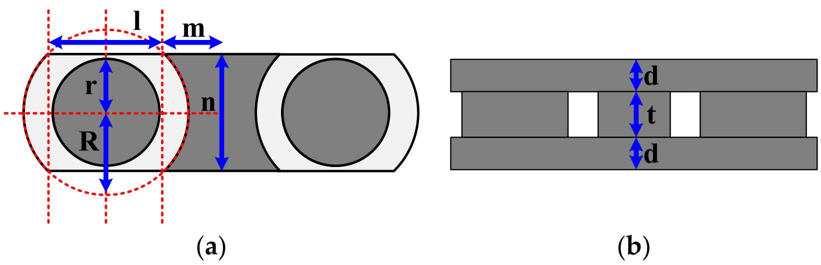

Figure 10. Diagram of the core size marking: (**a**) top and (**b**) side view.

The overall loss of the transformer can be divided into core loss and copper loss. Core loss is the product of core loss per unit volume and core volume, as shown in Equation (24). In Equation (25), Pv denotes the unit volume loss, and Cm, x, and y can be acquired from the core manufacturer's manual. Combining Equations (24) and (25) reveals that the core loss and volume Vel are related to the switching frequency fs and peak flux density B_{max}, with core loss being linearly proportional to Vel and exponentially proportional to fs and B_{max}. Next, B_{max} was expressed as Equation (26), where V_{in} denotes the input voltage, Ae represents the effective cross-sectional area of the core, and Np is the number of turns of the primary winding. In this study, the input voltage V_{in}, switching frequency fs, and effective cross-sectional area of the core are 400 V, 500 kHz, and 194 mm^2, respectively. The relationship between core loss and the number of primary-side turns is revealed through Equation (26), with a higher number of turns leading to a drop in peak flux density, reducing the core loss. However, from the perspective of copper loss, more turns resulted in greater loss. Thus, the optimal number of turns in this study was acquired by quantifying the core loss and copper loss.

$$Coreloss = Pcv \cdot Vel \tag{24}$$

$$Pv = Cm \cdot fs^{x} \cdot B_{\max}^{y} \tag{25}$$

$$B_{\max} = \frac{Vin}{4 \cdot Ae \cdot Np \cdot fs} \tag{26}$$

In this study, a full-bridge LLC resonant conversion topology was employed for the primary-side circuit architecture, whereas the secondary-side rectification architecture consisted of a full-bridge topology. The turns ratio of the transformer was calculated using Equation (27), and substituting the circuit specifications of this study (400 V input voltage and 300 V output voltage) yielded a transformer turns ratio of 4:3. However, the minimal number of turns on the primary side cannot be 1 because of the winding method of the adjustable leakage inductance, because the primary-side should be wound to the two outer legs, and because the primary side on both legs cannot be the same. Additionally, the winding ratio of the primary and secondary sides has to be an integer to prevent the need for a non-integer number of turns on the secondary side. Table 4 shows that the winding width of the core could be obtained by subtracting r from R, and the actual winding width was 5.5 mm.

$$n = \frac{Vin}{Vo} \tag{27}$$

Table 4. Parameter design of the asymmetric resonant tank.

Core Size	Value
Ae	194 mm^2
R	13.3 mm
r	7.8 mm
l	18.8 mm
m	7.29 mm
n	18.8 mm
d	6 mm
t	10.3 mm

The transformer turns ratio in this study was 4:3; thus, the number of turns at the primary and secondary sides could be 4:3, 8:6, 12:9, and so on. The core loss per unit volume (Pv) increased substantially when the peak flux density of the transformer exceeded 1000 G. Therefore, the peak flux density was designed to be less than 1000 G in the core turns design. Next, Equation (26) was rewritten as Equation (28), and $B_{\max}$ was set to 1000 G. According to Equation (28), the minimum number of winds on the primary side was 14.6. Practically, more windings mean more layers and greater costs.

Therefore, only the following five windings on the primary and secondary sides were considered: 16:12, 20:15, 24:18, 28:21, and 32:24.

$$Np > \frac{Vin}{4 \cdot Ae \cdot B_{\max} \cdot fs} = 14.6 \tag{28}$$

The peak flux density and core loss for different numbers of turns were obtained using Equations (24) and (26), and the results are plotted in Figure 11. The relationship between core loss and number of turns was nonlinear. The difference in core loss between 16 and 20 turns on the primary-side winding was 4.8 W, whereas 28 and 32 turns on the primary-side winding yielded a core loss of approximately 0.8 W. This was the main reason for designing $B_{\max}$ to be less than 1000 G.

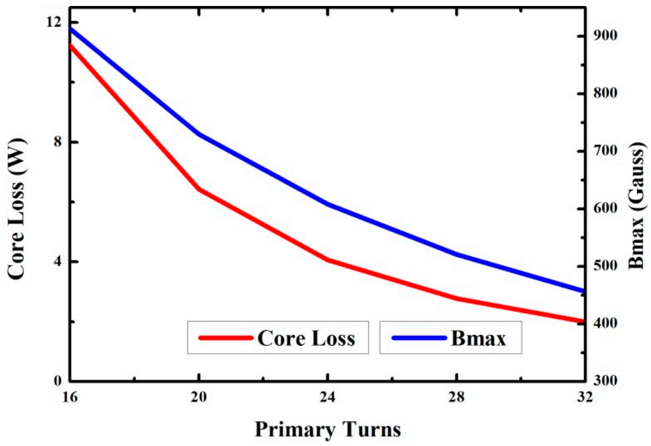

Figure 11. Peak flux density and core loss.

The high-frequency copper loss was analyzed next. Conventional transformers are mostly wound with litz wire; however, planar routing is more advantageous to utilize the window area of a transformer. Figure 12 compares the use of planar routing and four litz wires. Under the same condition of an occupied area of 4 mm^2, the cross-sectional area of the litz wires was 3.142 mm^2, whereas that of the planar routing was 4 mm^2 (Figure 12a,b, respectively); both yielded a 27% difference in DC resistance under the same length. Therefore, PCB routing was used as the transformer winding in this study to achieve high power density.

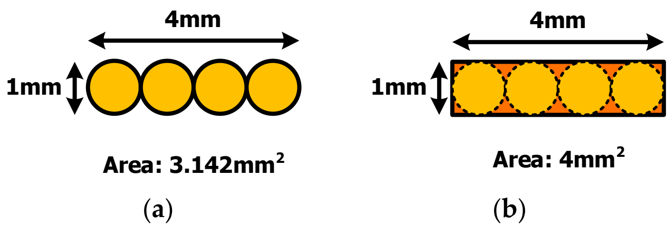

Figure 12. Winding usage in different transformers: (**a**) litz wire and (**b**) planar trace.

PCB routing was selected over litz wire under the same transformer window area because it resulted in lower DC resistance of the winding. However, a sharp rise in AC resistance loss was observed when the switching frequency was increased from the conventional 50 kHz–200 kHz to 500 kHz–1 MHz. Therefore, the AC resistance loss of the transformer winding was analyzed.

According to Dowell's equation, the skin effect and proximity effect can be expressed by Equations (29) and (30), respectively, where $\xi = h/\delta$, with h denoting the thickness of the copper wire in the transformer winding and δrepresenting the skin depth of the transformer winding. Additionally, m can be expressed using Equation (31), where e represents the number of winding layers. The five numbers of windings that were employed and the corresponding distributions of MMF are displayed in Figure 13.

Because the circuit architecture in this study was an LLC rather than bidirectional CLLC, only the leakage inductance on the primary side was adjusted. Therefore, the secondary side was wound around the two outer legs with the same or almost the same number of turns, and the primary and secondary sides were wound on an eight-layer PCB in an interleaved manner. A total of seven layers of PCB winding were used, and one layer was reserved as the routing that connected the two leg windings.

$$R_{ac\_skin} = \frac{\xi}{2} \cdot \frac{\sinh(\xi) + \sin(\xi)}{\cosh(\xi) - \cos(\xi)} \cdot R_{dc} \tag{29}$$

$$R_{ac\_proximity} = \frac{\xi}{2} \cdot (2m-1)^2 \cdot \frac{\sinh(\xi) - \sin(\xi)}{\cosh(\xi) + \cos(\xi)} \cdot R_{dc} \tag{30}$$

$$m = \left| \frac{MMF(e)}{MMF(e) - MMF(e-1)} \right| \tag{31}$$

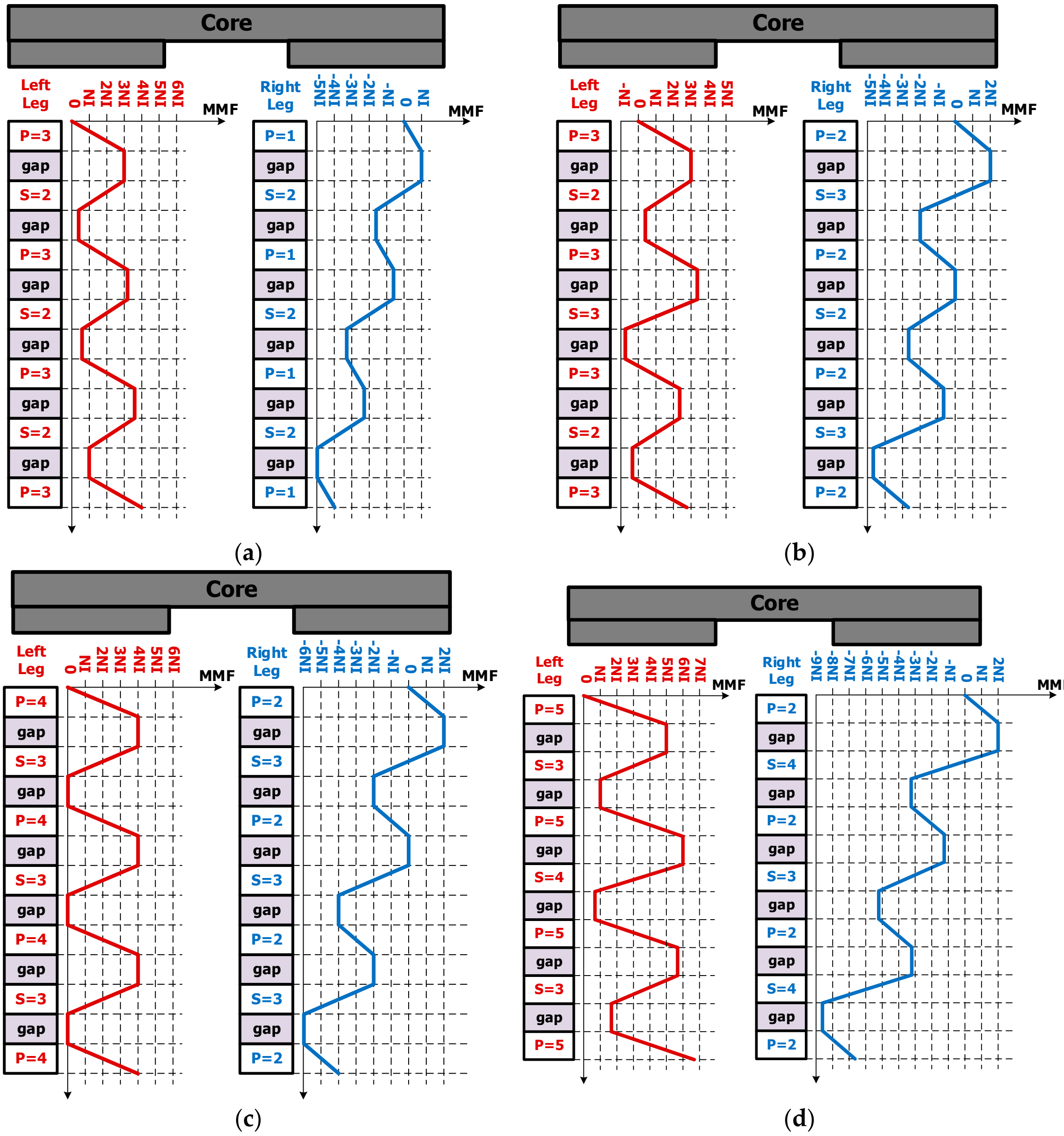

Figure 13. *Cont.*

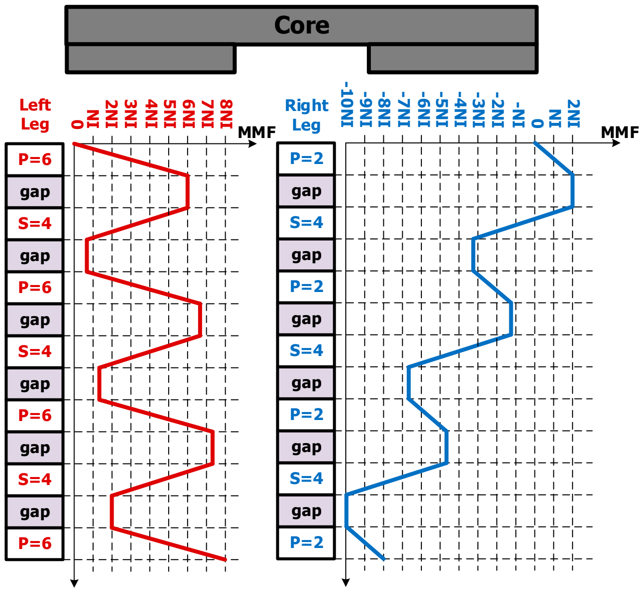

(**e**)

Figure 13. MMF distribution map of different numbers of windings: (**a**) Np = 16, Ns = 12; (**b**) Np = 20, Ns = 15; (**c**) Np = 24, Ns = 18; (**d**) Np = 28, Ns = 21; and (**e**) Np = 32, Ns = 24.

Figure 14 illustrates the copper loss and total loss of the transformer for different numbers of turns. The core loss could be obtained from Figure 11. More turns resulted in lower peak flux density of the core and thus lower core loss. However, more windings also led to greater copper loss, which could be divided into that associated with DC resistance and AC resistance. DC resistance was greater for more windings; however, the resistance that actually affects the high-frequency copper loss is AC resistance loss. Because an eight-layer board was used for transformer routing, more turns meant that each layer of the PCB board had to accommodate more windings, which narrowed the width of each winding. Moreover, according to Figure 13, more windings in each layer resulted in a higher MMF, causing substantially greater AC resistance under high frequency, which in turn resulted in greater copper loss. The various amounts of core loss and copper loss are presented in Table 5, and the results are plotted in Figure 14. Ultimately, the number of turns with the lowest total loss (24:18) was selected as the suitable number of turns of the transformer in this study. Figure 15 shows the peak flux density of the core, as simulated by ANSYS Maxwell software, to verify that the core operated normally.

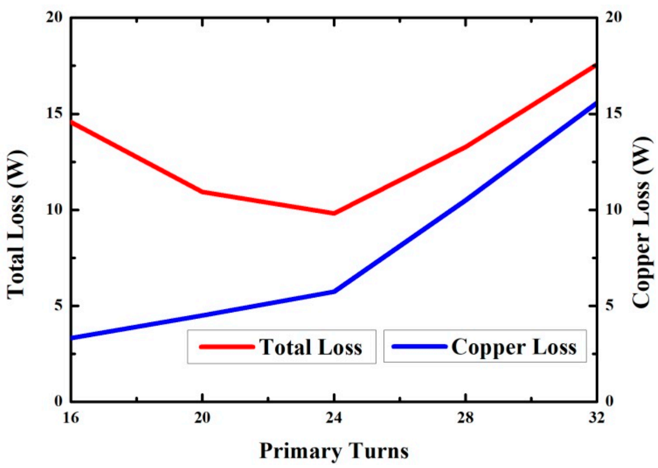

Figure 14. Copper loss and total loss.

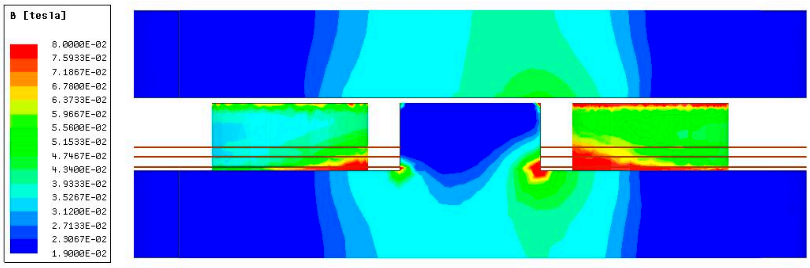

Figure 15. Flux density distribution by FEA 3D simulation.

Table 5. Parameter design of the asymmetric resonant tank.

Condition\Np:Ns	16:12	20:15	24:18	28:21	32:24
B_{max} (Gauss)	913	730	608	521	456
Core Loss (W)	11.23	6.43	4.07	2.77	1.99
Rdc (mΩ)	157	223	260	479	689
Rac (mΩ)	167	232	270	530	796
Copper Loss (W)	3.33	4.50	5.74	10.50	15.57
Total Loss (W)	14.56	10.93	9.81	13.27	17.55

4. Results

An LLC resonant converter with 1 kW output power and 500 kHz switching frequency was proposed in this study. Figure 16a,b shows the actual core size and circuit diagram, respectively. Table 6 details the components and design parameters used in this study.

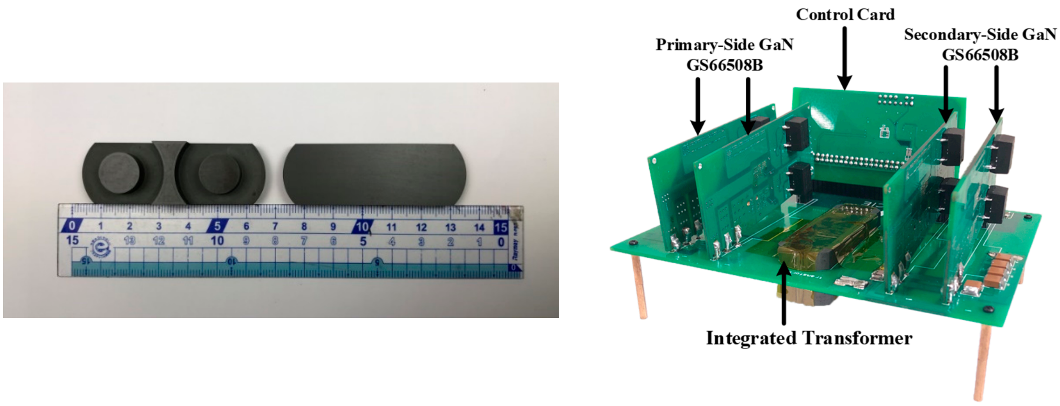

(**a**) (**b**)

Figure 16. Experimental prototype of the (**a**) core structure and (**b**) circuit.

Table 6. Parameter design of the asymmetric resonant tank.

Component	Value
Resonant and Operating Frequency	500 kHz
Transformer Turns Ratio	24:18
Transformer Material	3F36
Primary-Side Switch Device	GS66508B
Secondary-Side Switch Device	GS66508B
Primary-Side Driver	Si8271GB
Secondary-Side Driver	Si8271GB
Resonant Capacitor	22.4 nF
Leakage Inductance	4.7 µH
Magnetizing Inductance	80.5 µH

Figure 17 plots the measured conversion efficiency of the converter. The highest efficiency of 97.03% was achieved at 80% load. Figure 18 displays the circuit test waveform at full load, which includes the waveforms of Vds, Vgs, and the resonant current I_{Lr} of the primary-side power switch operating properly. Figure 19a–c shows temperature distribution of the primary-side power components at full load, with maximum temperatures of 38.1 °C, 40.4 °C, and 78.6 °C, respectively. Because the specifications of this paper are high-voltage to high-voltage, according to the loss analysis in Figure 4, the loss can be mainly attributed to the transformer, especially, on the transformer windings. Because the primary or secondary switching elements have zero-voltage-switch turn-on, the temperature distribution of the overall converter will be concentrated on the windings of the transformer.

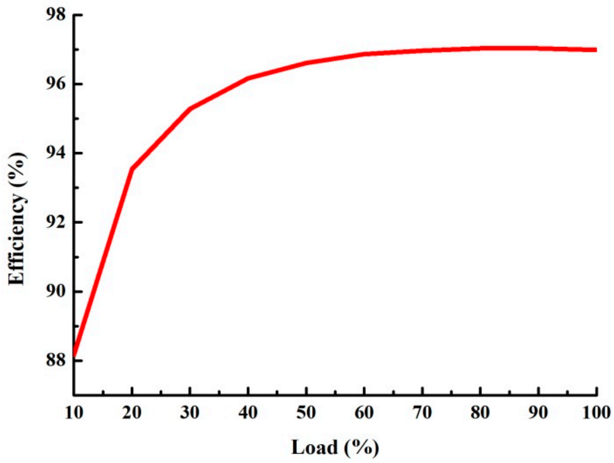

Figure 17. Measured power efficiency.

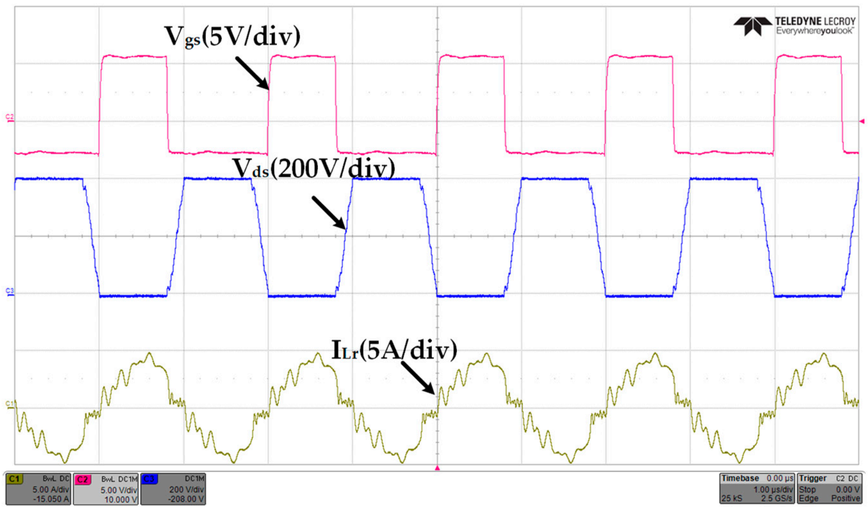

Figure 18. Experimental waveforms for the converter at full load.

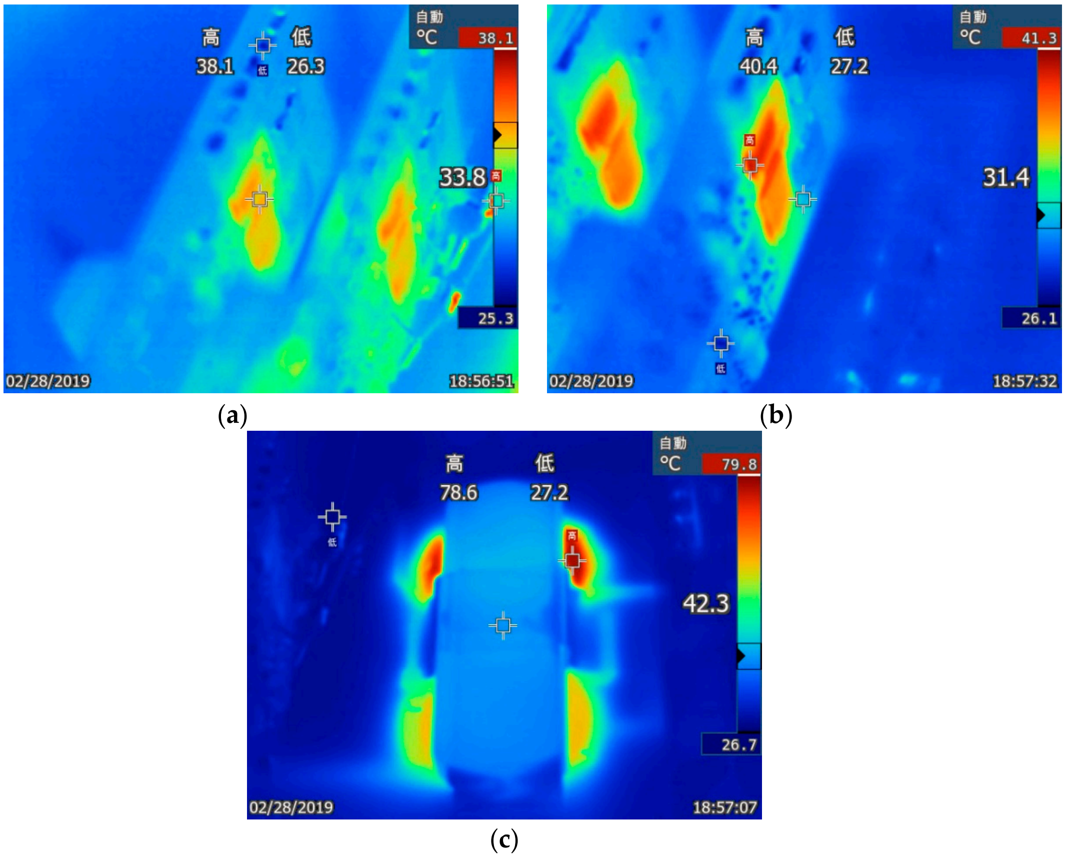

Figure 19. Temperature of the LLC converter at full load; (**a**) primary-side GaN devices, (**b**) secondary-side GaN devices, and (**c**) core and winding of transformer.

5. Conclusions

This study determined the primary-side topology and secondary-side rectification topology suitable for an LLC resonant converter under a switching frequency, input voltage, and output voltage of 500 kHz, 400 V, and 300 V, respectively. After loss analysis and determining the rated voltage and current of the components, the full-bridge topology was selected for both the primary and secondary sides. This study also investigated the small transformer leakage inductance caused by an interleaved winding structure, which was employed to reduce the winding MMF of the transformer under high-frequency switching. The adjustable leakage inductance structure was thus adopted in this study, and the influence of core shape on current distribution was explored. Subsequently, the feasibility of the core was verified through simulation using ANSYS Maxwell software. Ultimately, an LLC resonant converter with 1 kW output power and 500 kHz switching frequency was designed and tested. The results verified a maximum conversion efficiency of 97.03%.

Author Contributions: Y.-C.L., C.C., K.-D.C. and Y.-L.S. conceived and designed the prototype and experiments; C.C., K.-D.C., Y.-L.S. and M.-C. Tsai performed the experiments; Y.-C.L., C.C., K.-D.C. analyzed the data; Y.-C.L. contributed equipment/materials/analysis tools; Y.-C.L., C.C., K.-D.C. wrote the paper.

Funding: This work was supported in part by the Ministry of Science and Technology, Taiwan under Grant 107-2218-E-008 -012- and 107-2221-E-197 -030 -.

Conflicts of Interest: The authors declare no conflict of interest. The funders had no role in the design of the study; in the collection, analyses, or interpretation of the data; in the writing of the manuscript, or in the decision to publish the results.

References

1. Carli, R.; Dotoli, M.; Cianci, E. An optimization tool for energy efficiency of street lighting systems in smart cities. *IFAC-PapersOnLine* **2017**, *50*, 14460–14464. [CrossRef]
2. Pandharipande, A.; Caicedo, D. Smart indoor lighting systems with luminaire-based sensing: A review of lighting control approaches. *Energy Build.* **2015**, *104*, 369–377. [CrossRef]
3. Carli, R.; Dotoli, M.; Pellegrino, R. A decision-making tool for energy efficiency optimization of street lighting. *Comput. Oper.* **2018**, *96*, 223–235. [CrossRef]
4. Chen, X.; Huang, D.; Li, Q.; Lee, F.C. Multi-channel LED driver with CLL resonant converter. In Proceedings of the IEEE Energy Conversion Congress and Exposition (ECCE), Pittsburgh, PA, USA, 14–18 September 2014; pp. 3599–3606.
5. Shang, M.; Wang, H. A LLC type resonant converter based on PWM voltage quadrupler rectifier with wide output voltage. In Proceedings of the IEEE Applied Power Electronics Conference and Exposition (APEC), Tampa, FL, USA, 26–30 March 2017; pp. 1720–1726.
6. Liu, Y.-C.; Chen, K.-D.; Chen, C.; Syu, Y.-L.; Lin, G.-W.; Kim, K.A.; Chiu, H.-J. Quarter-Turn Transformer Design and Optimization for High Power Density 1-MHz LLC Resonant Converter. *IEEE Trans. Ind. Electron.* **2019**. [CrossRef]
7. Lu, J.L.; Hou, R.; Chen, D. Opportunities and design considerations of GaN HEMTs in ZVS applications. In Proceedings of the IEEE Applied Power Electronics Conference and Exposition (APEC), San Antonio, TX, USA, 4–8 March 2018; pp. 880–885.
8. Chen, R.; Brohlin, P.; Dapkus, D. Design and magnetics optimization of LLC resonant converter with GaN. In Proceedings of the IEEE Applied Power Electronics Conference and Exposition (APEC), Tampa, FL, USA, 26–30 March 2017; pp. 94–98.
9. Fei, C.; Gadelrab, R.; Li, Q.; Lee, F.C. High-Frequency Three-Phase Interleaved LLC Resonant Converter with GaN Devices and Integrated Planar Magnetics. *IEEE J. Emerg. Sel. Top. Power Electron.* **2019**, *7*, 653–663. [CrossRef]
10. He, P.; Khaligh, A. Comprehensive Analyses and Comparison of 1 kW Isolated DC–DC Converters for Bidirectional EV Charging Systems. *IEEE Trans. Transp. Electrif.* **2017**, *3*, 147–156. [CrossRef]
11. Dung, N.A.; Chiu, H.-J.; Lin, J.-Y.; Hsieh, Y.-C.; Chen, H.-T.; Zeng, B.-X.; Nguyen, D.A. Novel Modulation of Isolated Bidirectional DC–DC Converter for Energy Storage Systems. *IEEE Trans. Power Electron.* **2019**, *34*, 1266–1275. [CrossRef]
12. Huang, D.; Ji, S.; Lee, F.C. LLC resonant converter with matrix transformer. *IEEE Trans. Power Electron.* **2014**, *29*, 4339–4347. [CrossRef]
13. Mu, M.; Lee, F. Design and Optimization of a 380V-12V High-Frequency, High-Current LLC Converter with GaN Devices and Planar Matrix Transformers. *IEEE J. Emerg. Sel. Top. Power Electron.* **2016**, *4*, 1. [CrossRef]
14. Fei, C.; Lee, F.C.; Li, Q. High-Efficiency High-Power-Density LLC Converter with an Integrated Planar Matrix Transformer for High-Output Current Applications. *IEEE Trans. Ind. Electron.* **2017**, *64*, 9072–9082. [CrossRef]
15. Dowell, P. Effects of eddy currents in transformer windings. *Proc. Inst. Electr. Eng.* **1966**, *113*, 1387. [CrossRef]
16. Dixon, L.H. Eddy Current Losses in Transformer Winding and Circuit Wiring, Unitrode/TI Magnetics Design Handbook. 2000.
17. Ouyang, Z.; Hurley, W.G.; Andersen, M.A.E. Improved Analysis and Modelling of Leakage Inductance for Planar Transformers. *IEEE J. Emerg. Sel. Top. Power Electron.* **2018**. [CrossRef]
18. Liu, Y.-C.; Chen, C.; Lin, S.-Y.; Xiao, C.-Y.; Kim, K.A.; Hsieh, Y.-C.; Chiù, H.-J. Integrated magnetics design for a full-bridge phase-shifted converter. In Proceedings of the IEEE Applied Power Electronics Conference and Exposition, San Antonio, TX, USA, 4–8 March 2018; pp. 2110–2116.
19. Abu Bakar, M.; Bertilsson, K. An improved modelling and construction of power transformer for controlled leakage inductance. In Proceedings of the IEEE International Conference on Environment and Electrical Engineering (EEEIC), Florence, Italy, 7–10 June 2016; pp. 1–5.
20. Liu, G.; Li, D.; Zhang, J.Q.; Hu, B.; Jia, M.L. Bidirectional CLLC resonant DC-DC converter with integrated magnetic for OBCM application. In Proceedings of the IEEE International Conference on Industrial Technology (ICIT), Seville, Spain, 17–19 March 2015; pp. 946–951.

21. Li, B.; Li, Q.; Lee, F.C. A novel PCB winding transformer with controllable leakage integration for a 6.6kW 500kHz high efficiency high density bi-directional on-board charger. In Proceedings of the 2017 IEEE Applied Power Electronics Conference and Exposition (APEC), Tampa, FL, USA, 26–30 March 2017; pp. 2917–2924.
22. Li, B.; Li, Q.; Lee, F. High Frequency PCB Winding Transformer with Integrated Inductors for a Bi-directional Resonant Converter. *IEEE Trans. Power Electron.* **2019**, *34*, 6123–6135. [CrossRef]
23. Alonso, J.M.; Vina, J.; Vaquero, D.G.; Martinez, G.; Osorio, R. Analysis and Design of the Integrated Double Buck–Boost Converter as a High-Power-Factor Driver for Power-LED Lamps. *IEEE Trans. Ind. Electron.* **2012**, *59*, 1689–1697. [CrossRef]
24. Chen, W.; Hui, S.Y.R. Elimination of an Electrolytic Capacitor in AC/DC Light-Emitting Diode (LED) Driver with High Input Power Factor and Constant Output Current. *IEEE Trans. Power Electron.* **2012**, *27*, 1598–1607. [CrossRef]
25. Qiu, Y.; Wang, L.; Wang, H.; Liu, Y.-F.; Sen, P.C. Bipolar Ripple Cancellation Method to Achieve Single-Stage Electrolytic-Capacitor-Less High-Power LED Driver. *IEEE J. Emerg. Sel. Top. Power Electron.* **2015**, *3*, 698–713.
26. Ouyang, Z.; Thomsen, O.C.; Andersen, M.A.E. Optimal Design and Tradeoff Analysis of Planar Transformer in High-Power DC–DC Converters. *IEEE Trans. Ind. Electron.* **2012**, *59*, 2800–2810. [CrossRef]
27. Yang, B.; Lee, F.C.; Zhang, A.J.; Huang, G. LLC resonant converter for front end DC/DC conversion. In Proceedings of the IEEE Applied Power Electronics Conference and Exposition (Cat. No.02CH37335), Dallas, TX, USA, 10–14 March 2002; Volume 2, pp. 1108–1112.